# Evolution of iron carbides during tempering of low-alloy tool steel studied with polarized small angle neutron scattering, electron microscopy and

Citation for the original published paper (version of record):
Claesson, E., Magnusson, H., Kohlbrecher, J. et al (2022). Evolution of iron carbides during tempering of low-alloy tool steel studied with polarized
small angle neutron scattering, electron microscopy and atom probe. Materials Characterization, 194.
http://dx.doi.org/10.1016/j.matchar.2022.112464

Materials Characterization 194 (2022) 112464

Contents lists available at ScienceDirect

Materials Characterization

journal homepage: www.elsevier.com/locate/matchar

# Evolution of iron carbides during tempering of low-alloy tool steel studied with polarized small angle neutron scattering, electron microscopy and atom probe

Erik Claesson [a,b,*], Hans Magnusson [b], Joachim Kohlbrecher [c], Mattias Thuvander [d], Peter Hedström [b]

[a] Swerim AB, Box 7047, SE-16407 Kista, Sweden
[b] Dept. Material Science and Engineering, KTH Royal Institute of Technology, SE-100 44 Stockholm, Sweden
[c] Laboratory for Neutron Scattering, Paul Scherrer Institute, CH-5232 Villigen PSI, Switzerland
[d] Dept. of Physics, Chalmers University of Technology, SE-41296 Gothenburg, Sweden

ARTICLE INFO

*Keywords:*
Steel
Tempering
Precipitation
Carbides
Cementite
Martensite
SANS
SANSPOL
APT
STEM
EDS

ABSTRACT

The magnetic scattering of iron carbides in low-alloy tool steel was investigated ex-situ by polarized small angle neutron scattering measurements after tempering the steel at 550 °C and 600 °C. Magnetic features could be detected in the as-quenched sample resulting in a negative interference term, believed to be either $\theta$-$Fe_3C$, $\eta$-$Fe_2C$, or $\varepsilon$-$Fe_{2\text{-}3}C$. During tempering the evolution of cementite could be studied by the variation of the interference term and in $\gamma$-ratio, which is the ratio of the magnetic to nuclear scattering length density contrast. From scanning transmission electron microscopy (STEM) and atom probe tomography, it is evident that cementite ($\theta$-$Fe_3C$) is present directly when reaching the tempering temperature of either 550 °C or 600 °C. At longer tempering times, cementite gets enriched with substitutional elements like chromium and manganese, forming an enriched shell on the cementite particles. STEM and energy dispersive x-ray spectrometry show that the chemical composition of small cementite particles approaches that of Cr-rich $M_7C_3$ carbides after 24 h at 600 °C. It is also seen that small non-magnetic particles precipitate during tempering and these correspond well with molybdenum and vanadium-rich carbides.

## 1. Introduction

The industrial production route of commercial martensitic steel plates, used in construction or tooling applications, involves as final steps austenitization, quenching, and tempering. The tempering of these martensitic steels is carefully made to control the strength and toughness of the final products. The microstructural evolution of martensite during tempering is classified into different stages [1,2], which include: carbon redistribution to lattice defects and formation of pre-precipitation clusters [3], recovery of dislocation structures, decomposition of retained austenite [2], precipitation of $Fe_2C$-type transition carbides, cementite ($Fe_3C$), and alloy carbides. High martensite start temperature ($M_s$) and a limited quenching rate can result in the redistribution of carbon and carbide precipitation in the martensite already during quenching. This is referred to as auto-tempering (AT), with the formation of transition carbides such as eta ($\eta$) or epsilon ($\varepsilon$) [1,4], or the stable carbide cementite ($\theta$).

Carbon has a strong impact on the strength of martensitic steel grades [5]. In quenched-hardened steel, carbon can be in the form of carbides like AT carbides or segregated into solid solution clouds (Cottrell atmospheres) [6]. Cementite precipitates in most steels below 700 °C, i.e. in the equilibrium regime of ferrite, predominantly at martensitic lath boundaries if the martensite constituent has formed [1,7]. If the steel is exposed to high-temperature tempering around 500–600 °C substitutional alloying elements are activated by diffusion. For more alloyed steels, some or all the cementite particles dissolve and are replaced with more stable alloy carbides. For less alloyed steel without alloy carbides, partitioning of alloying elements takes place and elements like chromium and manganese dissolve in the iron carbides.

In low-alloyed steel grades, elements like chromium and manganese

---

* Corresponding author at: Swerim AB, Box 7047, SE-16407 Kista, Sweden.
*E-mail addresses:* erik.claesson@swerim.se (E. Claesson), hans.magnusson@swerim.se (H. Magnusson), joachim.kohlbrecher@psi.ch (J. Kohlbrecher), mattias.thuvander@chalmers.se (M. Thuvander), pheds@kth.se (P. Hedström).

https://doi.org/10.1016/j.matchar.2022.112464
Received 30 August 2022; Received in revised form 20 October 2022; Accepted 2 November 2022

are added to improve the final product properties, and to increase the hardenability and thereby the processability of the steel. Chromium can substitute iron in cementite [8], or stabilize chromium carbides like $M_7C_3$ and $M_{23}C_6$. Chromium together with manganese and silicon limits the cementite growth rate due to partitioning [9,10], where chromium and manganese are enriched in the cementite and silicon is rejected and enriched in the matrix at the matrix/cementite interface. This partitioning effect will lead to an accumulation of alloying elements at the edge of the particles [7]. The enrichment of chromium in cementite can thereby be a precursor for other carbides, which has been reported by Lerbacher et al. [2]. Similar observations were reported in the early work of Baker and Nutting [11], and Honeycombe and Seal [12].

Characterization of microstructural features in the nanometer size range with methods such as electron microscopy (EM) [7] and atom probe tomography (APT) [2] give very localized information. Small-angle scattering methods with either neutrons or x-rays, supported by EM and APT, make it possible to characterize larger sample volumes and get more statistics and a better idea about the general evolution of nanosized features during or after processing. This is especially useful if compared with mean-field computational modeling tools predicting a precipitation sequence when average data of phase fraction, number density, and particle size is needed. Polarized small-angle neutron scattering (SANSPOL) has been used in several previous studies to quantify the magnetic contribution of nanosized features [13–18]. Coppola et al. have performed SANSPOL experiments on steel samples [19,20], and have shown the presence of magnetic precipitates with a magnetic scattering length density that could be assigned to the cementite phase. SANSPOL experiments and analysis of the interference term are used to accurately determine the magnetic contrast with respect to the nuclear one, and thereby possibly identify the carbide type. Tool steels are thermodynamically complex with several different coexisting precipitate types. Separating the measured signal from these carbides with regular SANS can be difficult. SANSPOL is therefore a useful method to separate the signals by modifying the scattering contrast providing information that is not detectable with regular SANS, as will be shown in this work.

Cementite has been reported to be ferromagnetic at room temperature and to become paramagnetic above its Curie temperature [21]. The Curie temperature depends on the cementite composition and has been reported to vary by several degrees (173–187 °C) depending on the Fe/C ratio [21,22]. It is believed that the magnetic properties of cementite will change further during the partitioning sequence of chromium and manganese. Medvedeva et al. calculated that the total magnetization of cementite decreases with increasing chromium concentration [8]. Complementary data pointing in the same direction were presented by Shigematsu showing that the magnetic moment of cementite decreases from 1.9 $\mu_B$ for $Fe_3C$ to 0.4 $\mu_B$ for $(Fe_{0.799}Cr_{0.201})_3C$ [23]. A similar effect has been reported for manganese partitioning, decreasing the magnetization with increasing manganese content [24].

Several calculations have been reported to estimate the local magnetic moments [25–27]. Dick et al. calculated the average atomic magnetic moment of cementite as a function of temperature and estimated the average magnetic moment at 25 °C to be about 1.6 $\mu_B$ [25]. Higher values of $1.7 - 1.9$ $\mu_B$ per iron atom at 0 K have also been reported [23–25]. The magnetic properties of the transition carbides η and ε have also been studied. Lv et al. estimated the average magnetic moment of η-$Fe_2C$ by first principle calculations to be 1.1 $\mu_B$ or 1.3 $\mu_B$ depending on the model used, while it was calculated to be 0 for ε-$Fe_{2\text{-}3}C$ [28]. The different magnetic properties of cementite and transition carbides mean that the SANSPOL method can be used to study the evolution of transition carbides and cementite during the tempering of steels. This report focuses on the evolution of these carbides during tempering at 550–600 °C. The main interest is in the activation of alloying elements by diffusion giving a partitioning effect. Even though some studies have investigated the evolution of carbides in low alloy steel [29] the detailed understanding of the transitions between elemental clusters, transition carbides, cementite and alloy carbides is not well understood. SANSPOL measurements are supported by scanning transmission EM (STEM) and APT measurements in order to delineate the evolution of magnetic properties and chemical composition of the particles.

## 2. Material and methods

The studied low alloy steel was produced by the company SSAB. The chemical composition is given in Table 1. Samples were austenitized and quenched to room temperature (RT), and subsequently tempered at 550 and 600 °C for up to 24 h with intermediate steps of 0 h, 0.5 h, 1 h, and 4 h. The 0 h samples represent heating to tempering temperature and directly quenching to RT. The samples were put into the preheated furnace, and it took about 1 h for the material to reach the tempering temperature of 550 and 600 °C. Details about the manufacturing conditions have been explained in previous work [30].

### 2.1. Characterization

The STEM work was conducted using a Jeol 2100F operated at 200 kV and equipped with an Oxford X-MAXN 80TLE EDS detector. The carbon extraction replicas were prepared by polishing sample surfaces by standard methods. The polished surfaces were etched in 2% Nital solution for about 5 s. A 20 nm thin carbon film was sputtered onto the etched surface using a Gatan Precision Etching and Coating System. The carbon film was removed by immersing the sample surface in 10% Nital solution [30]. The EDS analysis was performed using line scans to study the chemical distribution around cementite particles after different tempering times, 0, 1, and 24 h at 550 °C and 600 °C.

APT was performed using a LEAP 3000× HR. The measurements were conducted in laser pulse mode, with a laser wavelength of 532 nm, pulsed with a frequency of 200 kHz. The laser pulse energy was 0.30 nJ, and the sample temperature was 50 K. The IVAS 3.6 software (Cameca) was used for data analysis. Samples for APT analysis were cut into thin strips and electropolished into needles shaped samples [30].

Ex-situ SANSPOL experiments were performed at the Swiss spallation neutron source SINQ and the SANS-I instrument [31], Paul Scherrer Institute (PSI, Villigen, Brugg, Switzerland). Experiments were conducted using a beam of cold neutrons made monochromatic by a velocity selector. The wavelength (λ) of the incident neutrons was 6 Å and the wavelength resolution ($\Delta\lambda/\lambda$) was 10%. A magnetic field of 1.5 T was applied perpendicular to the incident beam to separate the magnetic and nuclear scattering. The investigated Q-range was 0.03–2.5 $nm^{-1}$ corresponding to a particle size of about 1.3–100 nm in real space. All measurements were corrected regarding background, sample thickness, and sample transmission. The BerSANS software [32] was used for data reduction and the Sasfit software was used for model-dependent fitting [33].

### 2.2. Polarized small-angle neutron scattering (SANSPOL)

Unpolarized small angle neutron scattering (SANS) studies on steel samples are generally performed with an external magnetic field (H) applied perpendicular to the incident neutron beam making it possible to separate the nuclear and magnetic scattering. If the magnetic field is high enough to saturate the sample, all magnetic scattering $F_M^2$ will be directed perpendicular to the magnetic field. The nuclear scattering $F_N^2$, which is independent of the external magnetic field, can be assumed to be spherical symmetric (isotropic). The scattering intensity, in this case,

**Table 1**
Chemical composition of the studied steel in wt%.

| Fe | C | Si | Mn | Cr | Ni | Mo | V | Ti, Nb |
|---|---|---|---|---|---|---|---|---|
| Bal. | 0.3 | 1.1 | 0.81 | 1.5 | 1.4 | 1.1 | 0.13 | Traces |

can be described as:

$$I(Q) = F_N^2 + F_M^2 sin^2\alpha \tag{1}$$

Where α is the angle between the magnetic field and the scattering vector (Q). The magnetic or the nuclear form factors are given by $F_{\mathrm{N,M}} = \Delta\rho_{N,M}V^{pj}f(\mathrm{Q},R)$, where $\Delta\rho_{N,M}$ is the magnetic or nuclear scattering density contrast between the particle $j$ and the matrix, $V_{pj}$ is the particle volume and $f(\mathrm{Q},R)$ depends on the particle shape.

The nuclear scattering length density of a phase can be calculated by:

$$\rho_N^j = \sum \frac{x_i b_i}{v_i} \tag{2}$$

Where $x_i$ is the atom fraction of $i$, $b_i$ is the coherent scattering length of atom $i$, and $v_i$ is the atomic volume of $i$. The magnetic scattering length density can be calculated by the following equation:

$$\rho_M^j = \frac{p_0 u}{v} \tag{3}$$

Where $p_0 = 2.7 \cdot 10^{-15}$ m is a constant, $u$ is the mean atomic moment and $v$ is the mean volume per atom [34,35]. The nuclear and magnetic scattering length density contrast is the difference in the scattering lengths between the particle and the matrix, $\Delta\rho_{N,\ M} = \rho^p_{N,\ M} - \rho^m_{N,\ M}$.

In a small angle neutron scattering experiment with polarized neutrons (SANSPOL), a spin-flipper is used to align the neutron spins to be either antiparallel (+) or parallel (−) to the magnetic field H. The scattering is then the result of four different processes separated into two categories, non-spin-flip, or spin-flip processes. The non-spin-flip represents when the spin is preserved $|F^{++}|^2$ and $|F^{--}|^2$, and spin-flip when the spin of the incident neutron is flipped by the scattering $|F^{+-}|^2$ and $|F^{-+}|^2$ [36]. The measured neutron intensity, and its dependency on the polarization, define the SANSPOL method.

When the magnetic field H is applied to measure a monodisperse system with non-interacting particles, and when the magnetic moments are fully aligned i.e., both the magnetic moments and the neutron polarization are parallel to H, the intensities of both the non-spin-flip and spin-flip processes are given by:

$$I^+(Q) = \langle |F^{++}|^2 \rangle + \langle |F^{+-}|^2 \rangle = F_N^2 + \{F_M^2 - 2P(1-2f^+)F_N F_M\} sin^2\alpha \tag{4}$$

and

$$I^-(Q) = \langle |F^{--}|^2 \rangle + \langle |F^{-+}|^2 \rangle = F_N^2 + \{F_M^2 - 2P(1-2f^-)F_N F_M\} sin^2\alpha \tag{5}$$

$P$ is the degree of polarization, $P = (n^+ - n^-)/(n^+ + n^-)$, $f^{\pm}$ is the efficiency of the spin flipper. The reversal of the spins from + to – is close to unity when the spin-flipper is on ($f^- \approx 1$) and zero when the spin-flipper is off ($f^+ \approx 0$).

For polarization, the anisotropy of the scattering signals is like Eq. (1).

$$I^{\pm}(Q) = A(Q) + B^{\pm}(Q) sin^2\alpha \tag{6}$$

The isotropic part A(Q) is the nuclear scattering ($F_N^2$) and is independent of polarization. However, for polarized neutrons the anisotropic part $B^{\pm}(Q)$ is different for the two polarization states. $A(Q)$ and $B^{\pm}(Q)$ with N different precipitates in the system can be written as:

$$A(Q) = \sum_{i=1}^{n} F_{N,i}^2 \tag{7}$$

and

$$B^{\pm}(Q) = \sum_{i=1}^{n} \left(F_{M,i}^2 - 2P(1-2f^{\pm})F_{N,i}F_{M,i}\right) \tag{8}$$

The scattering intensity of polarized neutrons includes a magnetic-nuclear interference term, which is the difference in the intensities given by Eq. (4) and Eq. (5).

$$I^-(Q) - I^+(Q) = B_{int} sin\alpha^2 = 4Pf^- sin^2\alpha \sum_{i=1}^{n} F_{N,i}F_{M,i} \tag{9}$$

The interference term ($B_{int}$= $B^{-}(Q)$-$B^{+}(Q)$) is linear in the magnetic amplitude and it is, therefore, possible to determine the absolute value of the magnetic contrast (magnetic moment) depending on the nuclear contrast (compositions of particles) [36]. From Eq. (9) it is possible to determine the ratio between the magnetic and the nuclear form factors $\gamma = F_M/F_N$, which is proportional to the ratio of magnetic to nuclear scattering length density difference, $\Delta\rho_M/\Delta\rho_N$ [13,37].

From SANSPOL the $\gamma$-ratio, for a system with multiple types of precipitates, can be accurately determined by

$$\gamma - ratio = \frac{\sum_{i=1}^{n} F_{N,i}F_{M,i}}{4Pf^- \sum_{i=1}^{n} F_{N,i}^2} = \frac{F_M}{F_N} \tag{10}$$

## 3. Results

### 3.1. Carbide analysis with STEM

Representative micrographs taken on carbon extraction replicas for the as-quenched (AsQ) sample, and samples tempered at 600 °C for 0 and 24 h are presented in Fig. 1(a)-(c). Carbides are identified as bright features in the micrographs presented in Fig. 1. AT-carbides believed to be ε-carbides, together with (Ti, V, Nb)C, and large $Mo_6C$ were found in the as-quenched material. The latter, $Mo_6C$, is too large to be in the detected length scale (DLS) of the SANSPOL experiment [30]. However, both AT-carbides and (Ti, Nb, V)C highlighted in Fig. 1 (a), are in the DLS, both seen in between martensitic laths. Compositional measurements across the AT-carbides/$Fe_2C$ indicate that they are pure Fe-carbides, see Fig. 2. The AT-carbides are dissolved during heating to tempering temperatures (550° and 600 °C) and are replaced by cementite ($Fe_3C$) mainly formed at martensitic lath boundaries. The fraction and size of iron carbides, $Fe_3C$, increase with tempering time as seen in Fig. 1 (b) and (c).

Even though the nucleation and growth of cementite are rapid and assumed to start at low temperatures [1,7], the coarsening of the cementite appears to be restricted. The limited growth of cementite is believed to be caused by the partitioning of Cr forming an Cr enriched shell around the carbide. The partitioning of Cr could be studied with STEM-EDS and is demonstrated by the EDS mapping of a cementite particle in Fig. 3 (a). Maps of both Cr and Fe are shown after tempering at 550 °C for 24 h. A line scan on the same particle was performed and the elemental profile is plotted in Fig. 3 (b).

The partitioning of Cr was further studied by investigating the Cr/Fe ratio in line scans across the cementite particles. The resulting Cr/Fe ratios as a function of tempering time at 550 °C are presented in Fig. 4, giving profiles after 0 h, 1 h, and 24 h of tempering. In the 0 h sample, nearly no enrichment of chromium is seen in the iron carbide. However, already after 1 h, and especially after 24 h, there is a strong enrichment of chromium in the cementite. The corresponding Cr/Fe ratio according to thermodynamic equilibrium calculations, for cementite and $M_7C_3$, are presented as references. Calculations were made with Thermo-Calc using the steel database TCFE11. It should be noted that in the equilibrium calculations, some phases are excluded since they are never seen under practical heat treatment conditions for low-alloyed steels, like diamond and graphite. In this report also $M_{23}C_6$ is excluded since there is not enough time for it to form. Metastable carbides, in this case, cementite and $M_7C_3$, can be calculated and their composition evaluated under meta-equilibrium.

The corresponding results for samples tempered at 600 °C are presented in Fig. 5. In comparison to 550 °C, the Cr/Fe ratio increases much faster due to the higher temperature activating diffusion. The Cr/Fe ratio exceeds the equilibrium values for cementite and approaches the values for chromium carbide $M_7C_3$.

### 3.2. Atom probe tomography

Atom probe tomography was also used to study the compositional

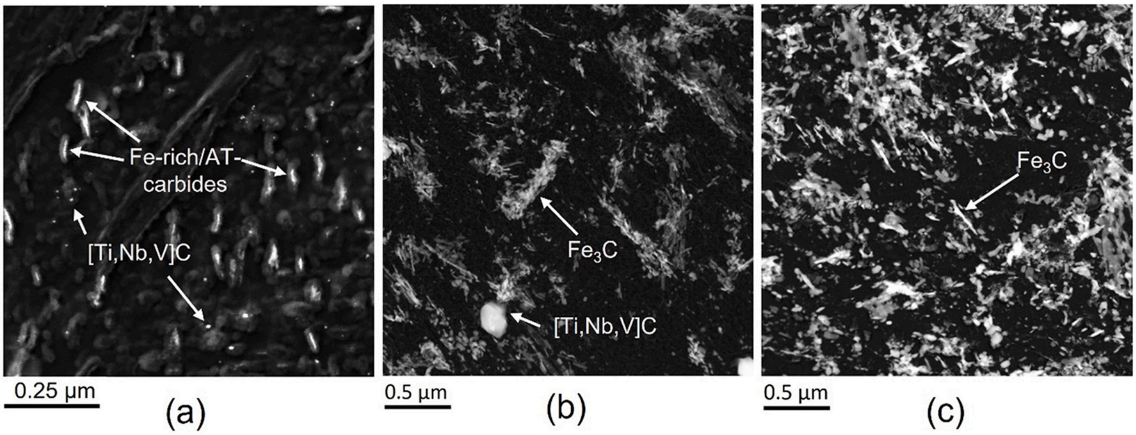

**Fig. 1.** Dark-field scanning transmission electron microscopy (STEM) micrographs showing carbides (bright areas) on carbon extraction replicas. (a) AsQ sample, (b) after tempering for 0 h at 600 °C and, (c) 24 h at 600 °C.

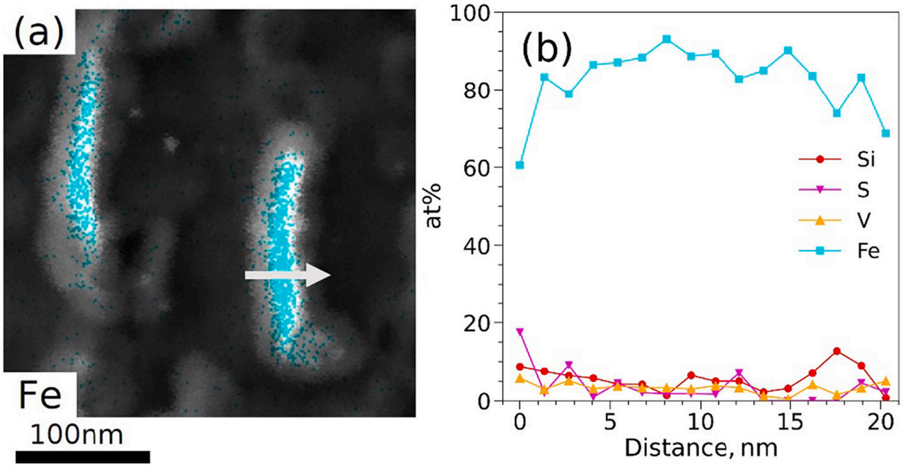

**Fig. 2.** (a) Iron (turquoise) mapping with EDS on AT-carbides in as-quenched condition (on an extraction replica). (b) Corresponding line scan of the particle indicated in (a), at.% plotted against distance. (For interpretation of the references to colour in this figure legend, the reader is referred to the web version of this article.)

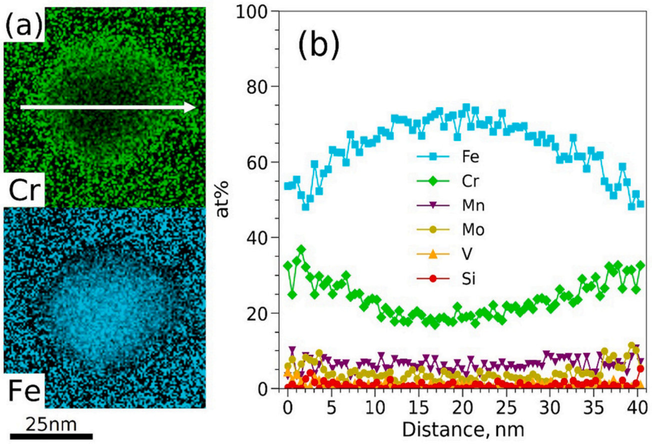

**Fig. 3.** (a) Mapping with EDS of iron and chromium in a cementite particle (on an extraction replica) after tempering at 550 °C for 24 h. (b) Corresponding line scan of the particle in (a), at.% plotted against distance.

evolution of cementite during tempering. Concentration profiles were generated using proximity histograms (proxigrams) created from isosurfaces. Results after 0 h at 600 °C are shown in Fig. 6(a)-(b) where (a) shows isosurfaces of C > 5 at.% and (b) the corresponding proxigram of large carbide highlighted in the reconstruction. The results show enrichment of Cr and Mn at the surface of the cementite particles, consistent with a core-shell structure of the M$_3$C. The peak values in the shell were 5.7 ± 0.1 at.% Cr and 2.9 ± 0.1 at.% Mn. It is also evident that the cementite particle has been enriched with Mo and V, and Si has been rejected from the particle and is enriched in the matrix at the matrix/cementite interface. The Cr and Mn contents, in both core and shell, are well below that of the equilibrium concentration of cementite at 600 °C. The measured carbon concentration is about 25 at.%, which agrees well with the predicted carbon concentration in cementite, M$_3$C. Both the size and shape of cementite particles correspond well with the carbides in the STEM analysis shown in Fig. 1 (b) and (c).

Fig. 6(c)-(d) shows isosurfaces of C > 5 at.% and corresponding proxigrams for cementite particle, the large carbide in the reconstructed volume, after tempering for 4 h at 600 °C. The Cr and Mn concentration has increased compared to the sample tempered for 0 h, to 7.3 ± 0.04 at.% Cr and 3.9 ± 0.03 at.% Mn.

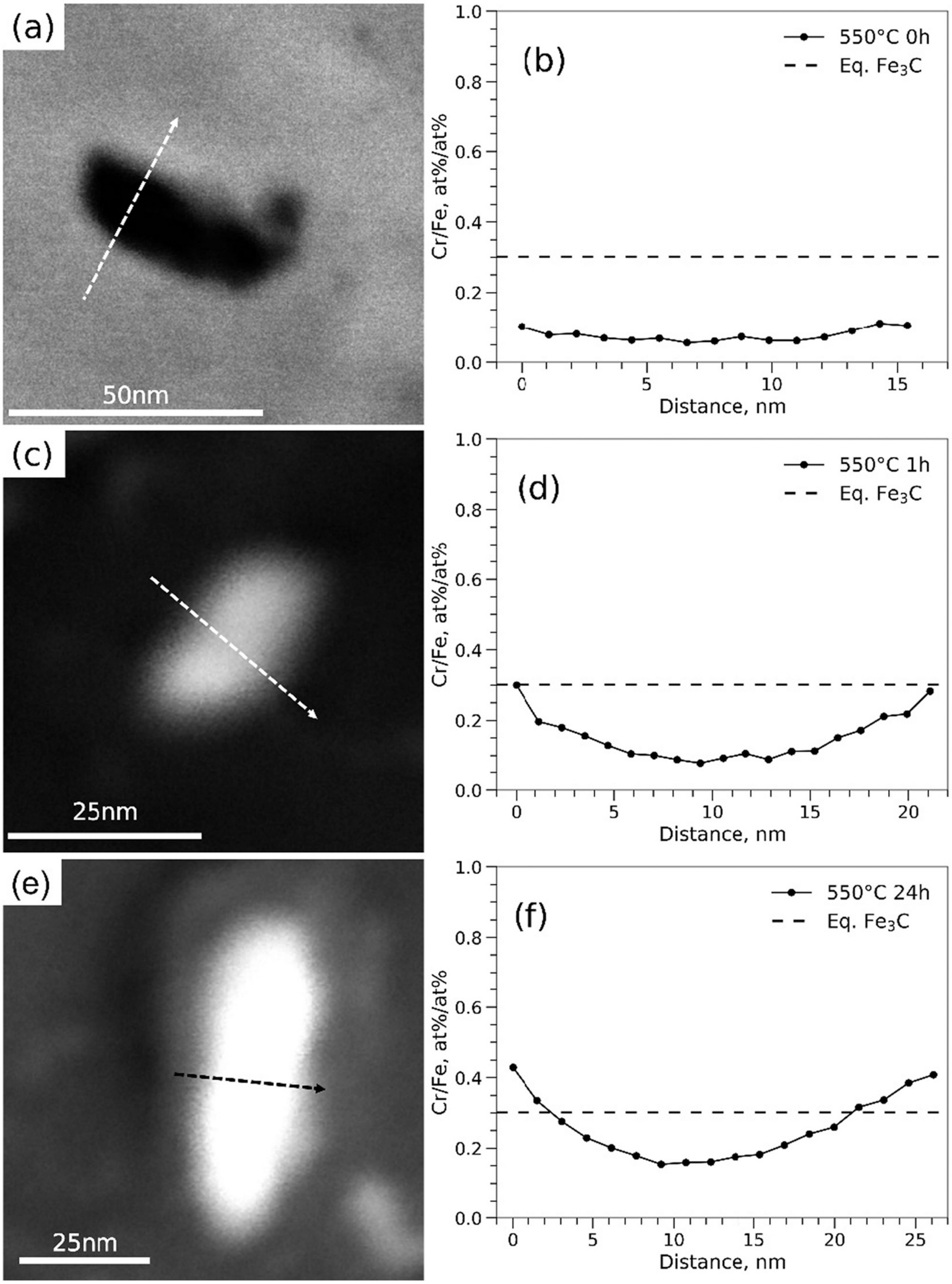

**Fig. 4.** Bright-field (a) and dark-field ((c) and (e)) images and STEM-EDS line-scan profiles of the metal content across iron carbides (on an extraction replica). The Cr/Fe-ratio is given after (a)-(b) heating to 550 °C, (c)-(d) 1 h at 550 °C and, (e)-(f) 24 h at 550 °C.

### 3.3. *SANSPOL*

Scattering curves for the flipper On and Off measurements perpendicular to the magnetic field for the as-quenched sample are given in Fig. 7(a). The intensity of the signal with the spin flipper Off ($I_{\perp}^{+}$), compared with spin flipper On ($I_{\perp}^{-}$), is higher for all Q, resulting in an overall negative intensity in the interference term On-Off, ($I_{\perp}^{-} - I_{\perp}^{+}$), see Fig. 7(b), the intensity is approaching 0 at high Q.

The scattering intensities, perpendicular to H, for the two polarization states and interference terms for samples tempered for 0 h, 1 h, and 24 h at 550 °C and 600 °C are shown in Fig. 8(a)-(c) and (d)-(f), respectively. For both temperatures, there is a strong dependency on tempering time on the appearance of the flipper On and Off signals and consequently the interference term. After reaching the tempering temperature of 550C the variation of the interference term at Q-values <0.5 $\text{nm}^{-1}$ corresponds well with the size of cementite. The interference term is initially negative but increases and becomes positive at longer tempering times at both 550 °C and 600 °C. This is believed to represent the chemical evolution of the cementite core, which influences both the nuclear and magnetic scattering length contrast (SLD). For Q values

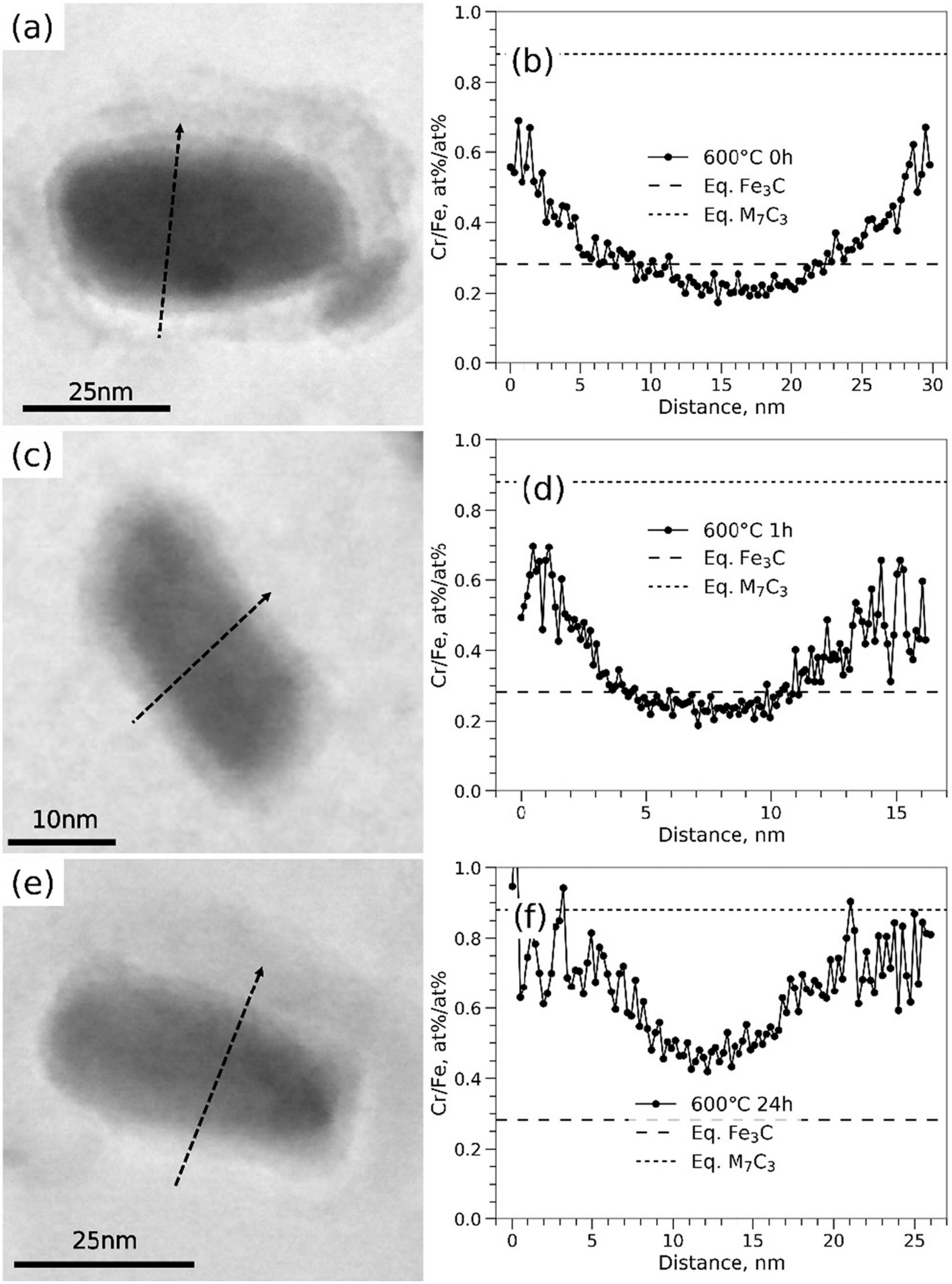

**Fig. 5.** Bright-field images and STEM-EDS line-scan profiles of the metal content across iron carbides (on an extraction replica). The Cr/Fe-ratio is given after (a)-(b) heating to 600 °C, (c)-(d) 1 h at 600 °C and, (e)-(f) 24 h at 600 °C.

$>0.5$ nm$^{-1}$, the interference term is positive and the Q-range corresponds well with the size of the cementite shell and nanosized secondary alloy carbides. This region is shifted towards lower Q with longer tempering times. There is a clear difference between the two temperatures, where the overall evolution of the scattering signals is faster at 600 °C compared to 550 °C.

The interference term and the corresponding γ-profile as a function of tempering time depend on the evolution in chemical composition, magnetic properties, and the average dimension of the formed precipitates. From the STEM-EDS and APT results, it is known that the AT-carbides consisted of Fe and C, with no dissolution of other alloying elements [30]. These AT-carbides are believed to be replaced by cementite when heating up to a tempering temperature, of 550 °C or 600 °C. With further heating, cementite particles get increasingly enriched in substitutional elements like Cr and Mn while Si is rejected. The evolution of cementite, both size, and composition, can be studied at low Q $< 0.5$ nm$^{-1}$. The composition of the cementite core and shell will influence the scattering length contrast, both magnetic and nuclear, which in turn will decide the sign of the interference term. Precipitation of nanosized secondary alloy carbides takes place at elevated temperatures, $>$ 500 °C, and since they are about 1–5 nm in diameter their evolution can be studied at high Q.

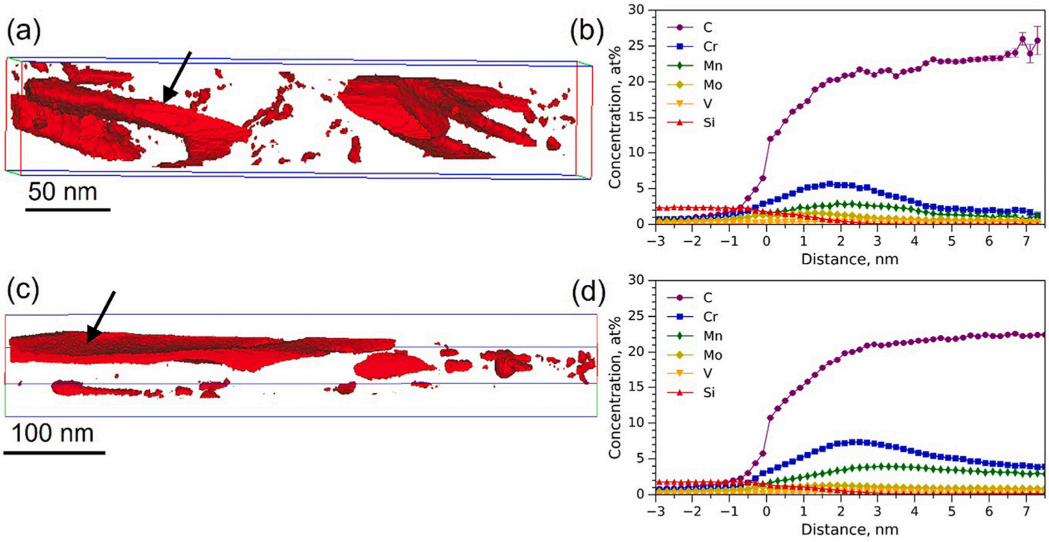

**Fig. 6.** Iso-surfaces and corresponding proxigrams of studied $Fe_3C$ carbides. The arrows points at the iso-surface from which the proxigram was generated. (a)-(b) carbide found in the sample heated to 600 °C and directly quenched in water (denoted 0 h). (c)-(d) results from carbides present after 4 h at 600 °C.

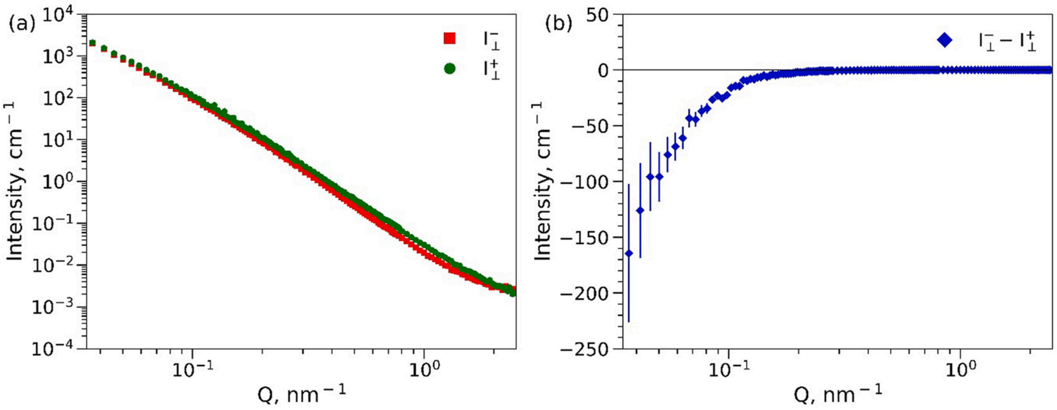

**Fig. 7.** 1D SANSPOL curves for the As-quenched material. Azimuthal average of sectors ±15° perpendicular to the magnetic field. (a) Polarization states and, (b) interference term.

For the AsQ sample both the interference term and $\gamma$ are negative over the whole explored Q-range as shown in Fig. 9(a) and (b), respectively. The $\gamma$-ratio is relatively constant at low Q which is believed to be related to the presence of AT-carbides ($Fe_2C$). A minimum of −0.8 in $\gamma$-ratio is found at $q = 0.75\ nm^{-1}$ corresponding to features with an average dimension (diameter) of about 4.2 nm.

After 0 h at 550 °C, $\gamma$ is negative at low Q and a minimum is found at $Q = 0.23\ nm^{-1}$, and the $\gamma$-ratio reverses its sign for $Q > 0.45\ nm^{-1}$. A maximum is reached at $Q = 1.4\ nm^{-1}$, which is believed to be related to the formation of secondary alloy carbides. With increased tempering time the maximum undergoes an overall increase, and the position is shifted towards lower Q, which is believed to be related to the change in composition and increase in particle size, respectively. The maximum is decreasing between 4 h and 24 h.

A similar trend can be seen for the minima at low Q. The $\gamma$-ratio is increasing with time and eventually becomes positive over the whole measured Q-range after 24 h, which is assumed to be related to the partitioning of substitutional elements in the cementite particle. The shift of the minimum towards lower Q with increasing tempering time is believed to be related to the overall growth of the cementite particles.

The evolution of the interference term and $\gamma$-ratio with increasing tempering time at 600 °C is shown in Fig. 10(a) and (b), respectively. Like the samples tempered at 550 °C, two regions, at low and high Q, are seen to have high magnetic correlations. The maximum at high Q reaches a constant value already after 0 h at 600 °C, which is interpreted as secondary alloy carbides reaching a steady composition. The position of the maximum is almost constant up to 4 h, and a clear shift towards lower Q can be seen first after 24 h, indicating a slow growth of the alloy carbides. As for the case at 550 °C, the minimum at low Q is negative after 0 h at 600 °C and is shifting towards lower Q at longer times. The $\gamma$-ratio also increases with increasing tempering time at 600 °C and becomes positive after about 1 h.

## 4. Discussion

Iron carbides in martensitic steel grades can precipitate during quenching due to auto-tempering. However, the type of iron carbide that forms depends on the martensite start temperature, the quenching rate, and the composition of the steel. The nucleation and growth processes of these carbides are complex and are believed to vary locally in the structure, possibly even between two neighboring martensite units. In commercially produced steel sheets it is difficult to prevent micro-segregation of both substitutional elements and carbon, which will be inherited by the final product [30]. This will influence the overall precipitation during processing, and likely also the precipitation of transition carbides, the latter by local variations in carbon content and

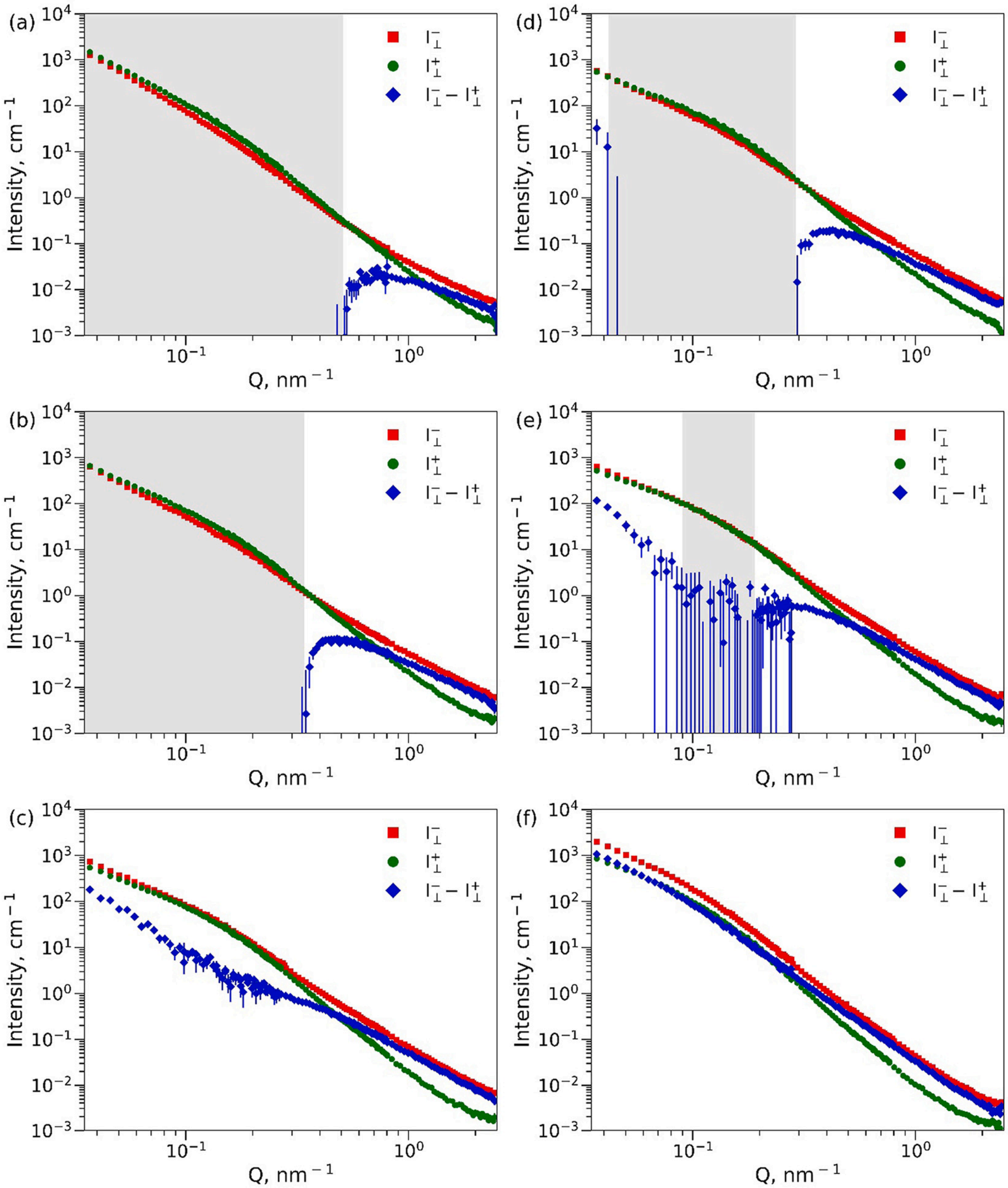

**Fig. 8.** 1D SANSPOL curves for the two polarization states and the interference term for (a) 0 h at 550 °C, (b) 1 h at 550 °C, (c) 24 h at 550 °C, (d) 0 h at 600 °C, (e) 1 h at 600 °C and (f) 24 h at 600 °C. Grey areas represent when the interference term is ≤0.

hardenability, which would influence the $M_s$-temperature. From STEM imaging it is seen that the AT-carbides appear as long thin plates within the laths, with a thickness within the detected q-range of the SANSPOL experiment. It is also believed that they do not undergo any significant spheroidization or coarsening before they are transformed to cementite upon tempering.

Time and temperature activate diffusion and give a more significant partitioning of Cr and Mn to the iron carbide, as demonstrated by STEM-EDS and APT results in this work. There is also some dependency on the carbide size since longer diffusion distances require more diffusion to equilibrate the carbide. Smaller carbides will more quickly reach an overall higher Cr/Fe ratio compared to larger carbides. This is illustrated in Fig. 11, which presents summarized STEM-EDS results of Cr/Fe ratios for tempering at 550 and 600 °C, for 1 and 24 h, depending on carbide size. A higher temperature of 600 °C more quickly increases the Cr/Fe ratio compared to tempering at 550 °C. However, for the largest particles, longer times are needed to further increase the Cr/Fe ratio in the particle core.

From the SANSPOL results for the AsQ sample, the interference term is negative for all Q, reaching zero at both ends of the Q range. This can be interpreted as having two features with a negative γ-ratio. The $\gamma - ratio = F_M/F_N$ is proportional to the ratio of magnetic to nuclear scattering length density difference, $\Delta\rho_M/\Delta\rho_N$. If the γ-ratio is negative either $\Delta\rho_M$ or $\Delta\rho_N$ is negative. These are believed to be features with a larger nuclear scattering length compared to the iron matrix. This is assumed since the magnetic scattering length of any carbide found in the samples is believed not to be larger than that of the Fe-matrix. Scattering length densities of V- and Mo-rich MC and $M_2C$ in the studied samples were calculated to be $3.53{\bullet}10^{-14}$ m$^{-2}$ and $5.44{\bullet}10^{-14}$ m$^{-2}$ respectively. The only carbides of relevance in the studied alloy that have a higher nuclear SLD are $Fe_3C$ $\rho_N^{Fe_3C} = 9.03{\bullet}10^{-14}$ m$^{-2}$, and $Fe_2C$ $\rho_N^{Fe_2C} = 9.56{\bullet}10^{-14}$ m$^{-2}$, compared to the corresponding value for the iron matrix $\rho_N^{matrix} = 7.82{\bullet}10^{-14}$ m$^{-2}$.

At low Q, γ is nearly constant. This behavior is believed to be

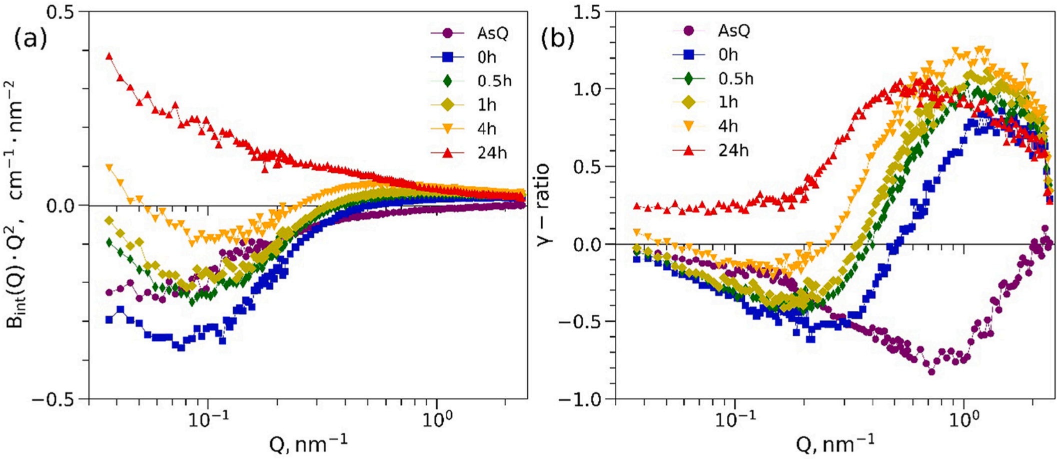

**Fig. 9.** (a) Kratky plot of the interference term for samples tempered at 550 °C and (b) the corresponding γ-ratio.

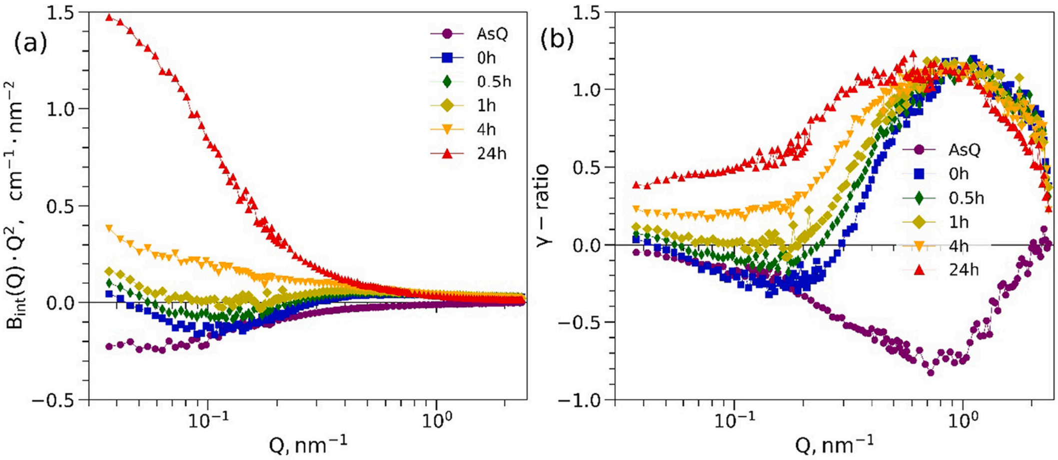

**Fig. 10.** (a) Kratky plot for the interference term for samples tempered at 600 °C. The corresponding γ-ratios are plotted in (b).

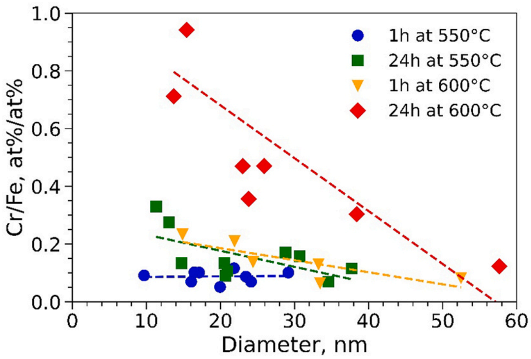

**Fig. 11.** Cr/Fe-ratio of the particle core from STEM-EDS line scans plotted against particle diameter of carbides formed during tempering at 550 °C and 600 °C. Each point represents one carbide.

representing AT-carbides. The minima at $\gamma = 0.75$ were found at $Q \approx 1$ $nm^{-1}$. The latter with an average dimension of 4–5 nm, which could correspond to the thickness of the carbides. It could also be that this minimum represents carbon clustering formed during quenching, which would be replaced early during tempering by the nucleation of cementite and later by secondary alloy carbides. This could not be concluded from the present study.

The partitioning of substitutional elements is believed to be seen in the SANSPOL results as well, where a clear change in the signal can be seen when comparing as-quenched material with material reheated to the tempering temperature (0 h at 600 °C). The minima in the γ-profiles shift towards lower Q with increasing tempering time at 550 °C, which is believed to be related to the growth of $M_3C$. The minima also increase with tempering time and become positive after 24 h. This is believed to be related to the change in composition and the enrichment of substitutional elements, e.g. chromium and manganese, which are known to lower the mean atomic magnetic moment of $M_3C$ [21,24]. However, the main reason for the change in the sign of the γ going from negative to positive at longer tempering times is the decrease in nuclear scattering length density due to the enrichment of substitutional elements. The Cr-rich shell of the cementite particle is believed to eventually result in an in-situ transformation of cementite to Cr-rich $M_7C_3$. However, this was not confirmed in this report.

With longer tempering times, secondary MC carbides rich in molybdenum and vanadium precipitate in these kinds of steels [1,11,12,30]. These particles are nonmagnetic and act as magnetic holes in the ferromagnetic Fe-matrix and hence do give a non-zero contribution to the magnetic scattering in the SANSPOL results. The nuclear scattering length contrast of the MC carbides is $3.53 \bullet 10^{-14}$ $m^{-2}$, which can be compared to reported values for iron matrix (BCC) close to $5 \bullet 10^{-14}$ $m^{-2}$ [19,34,35]. The γ-ratio is proportional to the ratio of the magnetic to nuclear contrast lengths, $\Delta\rho_M/\Delta\rho_N$. If assuming that both the magnetic and the nuclear scattering volumes and shapes are equal, and the matrix is magnetized to saturation, the γ-ratio depends solely on

$\Delta\rho_M/\Delta\rho_N$. For nonmagnetic MC at equilibrium composition, $\Delta\rho_M/\Delta\rho_N$ is calculated to be 1.17 which agrees well with the maximum γ-ratios at high Q in Fig. 9b) and Fig. 10b). For 550 °C tempering a maximum in γ-ratio is reached after 4 h, compared to 0 h for 600 °C tempering. Some MC carbides will undergo the MC to $M_2C$ transformation after further tempering [30], which is assumed to be the reason for the decrease in γ-ratio at 24 h for both tempering temperatures.

## 5. Conclusions

The evolution of carbide precipitates in low alloy steel has been analyzed using STEM-EDS, APT, and SANSPOL. From the experiments, the following conclusions can be drawn;

- Iron carbides were formed during quenching from austenite. The results indicate that they are transition carbides since they dissolve during heating to tempering temperature. Cementite was formed during heating to tempering temperature.
- STEM-EDS results revealed that cementite particles obtain a core-shell structure initially during tempering at 550 and 600 °C. The shell is mainly enriched in Cr. By studying the Cr/Fe ratio as a function of tempering it could be concluded that the concentration of Cr is increasing with tempering time and that the chemical composition of cementite approached that of $M_7C_3$ after tempering at 600 °C for 24 h.
- From APT it was concluded that cementitewas enriched in Cr during tempering, but also in Mn, Mo, and V while Si was rejected. Both the Cr and Mn concentrations in the cementite shell increased between heating to 600 °C and isothermal holding at 4 h at 600 °C.
- The results indicate that the formation of $Fe_3C$ and the partitioning of substitutional elements can be studied with SANSPOL. The magnetic properties of $M_3C$ change with tempering time due to the enrichment of substitutional elements at both the $M_3C$ core and the $M_3C$/matrix interface.
- Increasing tempering temperature by 50 °C, from 550 °C to 600 °C significantly accelerates the precipitation reaction which could be seen with both STEM-EDS and SANSPOL.

## Declaration of Competing Interest

The authors declare that they have no known competing financial interests or personal relationships that could have appeared to influence the work reported in this paper.

## Data availability

The raw/processed data required to reproduce these findings cannot be shared at this time as the data also forms part of an ongoing study.

## Acknowledgments

The authors acknowledge the financial support from the Swedish Foundation for Strategic Research under grant No. FID15-0043. SSAB Special Steel is gratefully acknowledged for the financial support, and for providing the experimental materials. This work is based on experiments performed at the Swiss spallation neutron source SINQ, Paul Scherrer Institute, Villigen, Switzerland.

## References

[1] G.R. Speich, W.C. Leslie, Tempering of steel, Metall. Trans. A. 3 (5) (1972) 1043–1054, https://doi.org/10.1007/BF02642436.

[2] C. Lerchbacher, S. Zinner, H. Leitner, Retained austenite decomposition and carbide formation during tempering a hot-work tool steel X38CrMoV5-1 studied by dilatometry and atom probe tomography, Metall. Mater. Trans. A Phys. Metall. Mater. Sci. 43 (13) (2012) 4989–4998, https://doi.org/10.1007/s11661-012-1358-3.

[3] B. Hutchinson, et al., Microstructures and hardness of as-quenched martensites (0.1-0.5%C), Acta Mater. 59 (14) (2011) 5845–5858, https://doi.org/10.1016/j.actamat.2011.05.061.

[4] G.R. Speich, Tempering of low-carbon martensite, Trans. Metall. Soc. AIME 245 (1969) 2553–2564.

[5] R.A. Grange, C.R. Hribal, L.F. Porter, Hardness of tempered martensite in carbon and low-alloy steels, Met. Trans. A 8 A (11) (1977) 1775–1785, https://doi.org/10.1007/BF02646882.

[6] M. Thuvander, H. Magnusson, U. Borggren, Carbide precipitation in a low alloyed steel during aging studied by atom probe tomography and thermodynamic modeling, Metals (Basel) 11 (12) (2021), https://doi.org/10.3390/met11122009.

[7] Z. Hou, R.P. Babu, P. Hedström, J. Odqvist, Early stages of cementite precipitation during tempering of 1C–1Cr martensitic steel, J. Mater. Sci. 54 (12) (2019) 9222–9234, https://doi.org/10.1007/s10853-019-03530-8.

[8] N.I. Medvedeva, I.R. Shein, M.A. Konyaeva, A.L. Ivanovskii, Effect of chromium on the electronic structure and magnetic properties of cementite, Phys. Met. Metallogr. 105 (6) (2008) 568–573, https://doi.org/10.1134/S0031918X08060069.

[9] G. Miyamoto, J.C. Oh, K. Hono, T. Furuhara, T. Maki, Effect of partitioning of Mn and Si on the growth kinetics of cementite in tempered Fe-0.6 mass% C martensite, Acta Mater. 55 (15) (2007) 5027–5038, https://doi.org/10.1016/j.actamat.2007.05.023.

[10] T. Sakuma, N. Watanabe, T. Nishizawa, The effect of alloying element on the coarsening behavior of cementite particles in ferrite, Trans. Jpn. Inst. Met. 21 (3) (1980) 159–168, https://doi.org/10.2320/matertrans1960.21.159.

[11] R. Baker, J. Nutting, The tempering of 2.25%Cr-l%Mo steel after quenching and normalizing, J. Iron Steel Inst. 192 (1959) 257–268 [Online]. Available: http://scholar.google.com/scholar?hl=en&btnG=Search&q=intitle:The+tempering+of+Mo+steel+after+quenching+and+normalizing#0.

[12] R.W.K. Honeycombe, A.K. Seal, The effect of some minor elements on the carbides precipitated during tempering, Iron Steel Inst. Spec. Rep. 64 (Precipitation processes in steels) (1959) 44–56.

[13] I. Bergenti, A. Deriu, L. Savini, E. Bonetti, F. Spizzo, H. Hoell, Small angle polarised neutron scattering investigation of magnetic nanoparticles, J. Magn. Magn. Mater. 262 (1) (2003) 60–63, https://doi.org/10.1016/S0304-8853(03)00019-2.

[14] A. Wiedenmann, Small-angle neutron scattering investigations of magnetic nanostructures and interfaces using polarized neutrons, Phys. B 297 (3) (2001) 226–233, https://doi.org/10.1016/S0921-4526(00)00872-3.

[15] V.S. Raghuwanshi, R. Harizanova, D. Tatchev, A. Hoell, C. Rüssel, Structural analysis of Fe-Mn-O nanoparticles in glass ceramics by small angle scattering, J. Solid State Chem. 222 (2015) 103–110, https://doi.org/10.1016/j.jssc.2014.11.009.

[16] M. Kammel, A. Hoell, A. Wiedenmann, Structure of magnetite ferrofluids investigated by SANS with polarized neutrons, Scr. Mater. 44 (8–9) (2001) 2341–2345, https://doi.org/10.1016/S1359-6462(01)00771-0.

[17] A. Wiedenmann, M. Kammel, A. Heinemann, U. Keiderling, Nanostructures and ordering phenomena in ferrofluids investigated using polarized small angle neutron scattering, J. Phys. Condens. Matter 18 (38) (2006), https://doi.org/10.1088/0953-8984/18/38/S13.

[18] A. Wiedenmann, Magnetic and crystalline nanostructures in ferrofluids as probed by small angle neutron scattering, Ferrofluids (2002) 33–58.

[19] R. Coppola, R. Kampmann, M. Magnani, P. Staron, Microstructural investigation, using polarized neutron scattering, of a martensitic steel for fusion reactors, Acta Mater. 46 (15) (1998) 5447–5456, https://doi.org/10.1016/S1359-6454(98)00189-X.

[20] R. Coppola, C.D. Dewhurst, R. Lindau, R.P. May, A. Möslang, M. Valli, Polarised SANS study of microstructural evolution under neutron irradiation in a martensitic steel for fusion reactors, Phys. B Condens. Matter 345 (1–4) (2004) 225–230, https://doi.org/10.1016/j.physb.2003.11.060.

[21] H.K.D.H. Bhadeshia, Cementite, Int. Mater. Rev. 65 (1) (2020) 1–27, https://doi.org/10.1080/09506608.2018.1560984.

[22] D. Walker, J. Li, B. Kalkan, S.M. Clark, Thermal, compositional, and compressional demagnetization of cementite, Am. Mineral. 100 (11–12) (2015) 2610–2624, https://doi.org/10.2138/am-2015-5306.

[23] T. Shigematsu, Magnetic properties of cementite (Fe1-xMex)3C, (me; Cr or Ni), J. Phys. Soc. Jpn. 37 (4) (1974), https://doi.org/10.1143/JPSJ.37.940.

[24] J. Von Appen, B. Eck, R. Dronskowski, A density-functional study of the phase diagram of cementite-type (Fe,Mn)3C at absolute zero temperature, J. Comput. Chem. 31 (14) (2010) 2620–2627, https://doi.org/10.1002/jcc.21557.

[25] A. Dick, F. Körmann, T. Hickel, J. Neugebauer, Ab initio based determination of thermodynamic properties of cementite including vibronic, magnetic, and electronic excitations, Phys. Rev. B - Condens. Matter Mater. Phys. 84 (12) (2011) 1–9, https://doi.org/10.1103/PhysRevB.84.125101.

[26] A.K. Arzhnikov, L.V. Dobysheva, Structural peculiarities of plastically-deformed cementite and their influence on magnetic characteristics and Mossbauer parameters, Solid State Commun. 146 (1–2) (2008) 102–104, https://doi.org/10.1016/j.ssc.2007.12.028.

[27] J.H. Jang, I.G. Kim, H.K.D.H. Bhadeshia, Substitutional solution of silicon in cementite: a first-principles study, Comput. Mater. Sci. 44 (4) (2009) 1319–1326, https://doi.org/10.1016/j.commatsci.2008.08.022.

[28] Z.Q. Lv, S.H. Sun, P. Jiang, B.Z. Wang, W.T. Fu, First-principles study on the structural stability, electronic and magnetic properties of Fe2C, Comput. Mater. Sci. 42 (4) (2008) 692–697, https://doi.org/10.1016/j.commatsci.2007.10.007.

[29] T. Zhou, J. Lu, P. Hedström, Mechanical behavior of fresh and tempered martensite in a CrMoV-alloyed steel explained by microstructural evolution and strength

modeling, Metall. Mater. Trans. A Phys. Metall. Mater. Sci. 51 (10) (2020) 5077–5087, https://doi.org/10.1007/s11661-020-05922-x.

[30] E. Claesson, et al., Carbide precipitation during processing of two low-alloyed martensitic tool steels with 0.11 and 0.17 V/Mo ratios studied by neutron scattering, electron microscopy and atom probe, Metals (Basel) 12 (5) (2022), https://doi.org/10.3390/met12050758.

[31] J. Kohlbrecher, W. Wagner, The new SANS instrument at the Swiss spallation source SINQ, J. Appl. Crystallogr. 33 (3 I) (2000) 804–806, https://doi.org/10.1107/S0021889800099775.

[32] U. Keiderling, H.M.I. Berlin, “ BerSANS ” Data Reduction Manual, Berlin, 2000.

[33] J. Kohlbrecher, User Guide for the SASfit Software Package SASfit : A Program for Fitting Simple Structural Models to Small Angle Scattering Data Joachim Kohlbrecher, Villigen, Switzerland, 2013 [Online]. Available: https://kur.web.psi.ch/sans1/SANSSoft/sasfit.html.

[34] Y.Q. Wang, et al., Investigating nano-precipitation in a V-containing HSLA steel using small angle neutron scattering, Under Rev. Acta Mater. 145 (2018) 84–96, https://doi.org/10.1016/j.actamat.2017.11.032.

[35] T. Dorin, K. Wood, A. Taylor, P. Hodgson, N. Stanford, Quantitative examination of carbide and sulphide precipitates in chemically complex steels processed by direct strip casting, Mater. Charact. 112 (2016) 259–268, https://doi.org/10.1016/j.matchar.2015.12.028.

[36] A.R. Beig, Wien, et al., Ferrofluids - Magnetically Controllable Fluids and Their Applications, 2002.

[37] A. Wiedenmann, Small-angle neutron scattering investigations of magnetic nanostructures using polarized neutrons, J. Appl. Crystallogr. 33 (2) (2000) 428–432.